



UNIVERSITY OF LEEDS

This is a repository copy of *Topological surface transport in epitaxial SnTe thin films grown on Bi<sub>2</sub>Te<sub>3</sub>*.

White Rose Research Online URL for this paper:  
<http://eprints.whiterose.ac.uk/130694/>

Version: Published Version

---

**Article:**

Taskin, AA, Yang, F, Sasaki, S [orcid.org/0000-0002-8915-6735](https://orcid.org/0000-0002-8915-6735) et al. (2 more authors)  
(2014) Topological surface transport in epitaxial SnTe thin films grown on Bi<sub>2</sub>Te<sub>3</sub>. *Physical Review B*, 89 (12). 121302. ISSN 1098-0121

<https://doi.org/10.1103/PhysRevB.89.121302>

---

**Reuse**

Items deposited in White Rose Research Online are protected by copyright, with all rights reserved unless indicated otherwise. They may be downloaded and/or printed for private study, or other acts as permitted by national copyright laws. The publisher or other rights holders may allow further reproduction and re-use of the full text version. This is indicated by the licence information on the White Rose Research Online record for the item.

**Takedown**

If you consider content in White Rose Research Online to be in breach of UK law, please notify us by emailing [eprints@whiterose.ac.uk](mailto:eprints@whiterose.ac.uk) including the URL of the record and the reason for the withdrawal request.



[eprints@whiterose.ac.uk](mailto:eprints@whiterose.ac.uk)  
<https://eprints.whiterose.ac.uk/>

## Topological surface transport in epitaxial SnTe thin films grown on Bi<sub>2</sub>Te<sub>3</sub>

A. A. Taskin,<sup>\*</sup> Fan Yang, Satoshi Sasaki, Kouji Segawa, and Yoichi Ando<sup>†</sup>

*Institute of Scientific and Industrial Research, Osaka University, Ibaraki, Osaka 567-0047, Japan*

(Received 5 May 2013; published 17 March 2014)

The topological crystalline insulator SnTe has been grown epitaxially on a Bi<sub>2</sub>Te<sub>3</sub> buffer layer by molecular beam epitaxy. In a 30-nm-thick SnTe film, *p*- and *n*-type carriers are found to coexist, and Shubnikov–de Haas oscillation data suggest that the *n*-type carriers are Dirac fermions residing on the SnTe (111) surface. This transport observation of the topological surface state in a *p*-type topological crystalline insulator became possible due to a downward band bending on the free SnTe surface, which appears to be of intrinsic origin.

DOI: [10.1103/PhysRevB.89.121302](https://doi.org/10.1103/PhysRevB.89.121302)

PACS number(s): 73.25.+i, 71.18.+y, 72.20.My, 73.20.At

The energy band inversion and time-reversal symmetry (TRS) are the main ingredients for realizing a nontrivial topology in  $Z_2$  topological insulators (TIs) [1–4]. Recently, the family of TIs has been extended by the introduction of topological crystalline insulators [5,6] where the topology is protected by a point-group symmetry of the crystal lattice rather than by TRS. The first material predicted to be a TCI was SnTe [6], in which the band inversion at an even number of time-reversal-invariant momenta (TRIMs) leads to a trivial  $Z_2$  topological invariant, but its mirror symmetry gives rise to a nontrivial mirror Chern number  $n_M = -2$  to guarantee the existence of topologically protected gapless surface states (SSs) on any surface containing a mirror plane. Angle-resolved photoemission spectroscopy (ARPES) experiments have confirmed the existence of Dirac-like SSs on the (001) surface of SnTe [7] and related compounds [8,9], generating a lot of interest in TCIs [10,11]. Naturally, an important next step is to elucidate the topological SSs with transport experiments, as was done for  $Z_2$  TIs [12–21].

However, probing the SSs in SnTe by transport experiments is a challenge, because of a high concentration of bulk holes ( $10^{20}$  to  $10^{21}$  cm<sup>-3</sup>) [22]. Nevertheless, in thin films, an enhanced surface-to-bulk ratio and a high surface mobility expected for topologically-protected SSs [23,24] might make it possible to probe them in quantum oscillations. To obtain high-quality thin films by molecular beam epitaxy (MBE) [25–32], lattice matching of the substrate is crucial. In this regard, while BaF<sub>2</sub> is the usual choice of substrate for SnTe [33] with its  $\sim 1.6\%$  lattice matching, we noticed that rhombohedral Bi<sub>2</sub>Te<sub>3</sub> may be a better choice, at least for the (111) growth direction, with the lattice matching of  $\sim 1.5\%$ . Furthermore, the building block of Bi<sub>2</sub>Te<sub>3</sub> is a Te-Bi-Te-Bi-Te quintuple layer (QL) terminated with a hexagonal Te plane, which naturally accommodates the Sn layer of the SnTe in the (111) plane [see Fig. 1(d)].

Here, we show that high-quality SnTe thin films can indeed be grown by MBE on Bi<sub>2</sub>Te<sub>3</sub> and that they are actually suitable for probing the topological SSs in transport experiments. Those films present Shubnikov–de Haas (SdH) oscillations composed of two close frequencies, whose dependence on the magnetic-field direction signifies that the observed oscillations stem from two-dimensional (2D) Fermi

surfaces (FSs). Furthermore, the phase of the oscillations indicates that the 2D carriers are Dirac electrons bearing the Berry phase of  $\pi$ . Measurements of the *I*-*V* characteristics across the SnTe/Bi<sub>2</sub>Te<sub>3</sub> interface and careful considerations of the energy-band diagram in this heterostructure lead us to conclude that the Dirac electrons reside on the top surface of SnTe.

The MBE growth was performed in an ultrahigh vacuum chamber with the base pressure better than  $5 \times 10^{-8}$  Pa. Before deposition of SnTe, a thin layer of high-quality Bi<sub>2</sub>Te<sub>3</sub> was grown under Te-rich conditions on sapphire substrates [34] with a two-step deposition procedure similar to that used for Bi<sub>2</sub>Se<sub>3</sub> films [27,29,35]. Both Bi (99.9999%) and Te (99.9999%) were evaporated from standard Knudsen cells. The Te<sub>2</sub>(Te<sub>4</sub>)/Bi flux ratio was kept at  $\sim 20$ . The growth rate, which is determined by the Bi flux, was kept at 0.3 nm/min. After growing  $\sim 30$  nm of the Bi<sub>2</sub>Te<sub>3</sub> layer, Sn (99.999%) and Te were co-evaporated, keeping the Te<sub>2</sub>(Te<sub>4</sub>)/Sn flux ratio at  $\sim 40$ , substrate temperature at 300 °C, and the growth rate at 0.4 nm/min. The resistivity  $\rho_{xx}$  and the Hall resistivity  $\rho_{yx}$  of the films were measured in a Hall-bar geometry by a standard six-probe method on rectangular samples on which the contacts were made with silver paste or indium near the perimeter. The magnetic field was swept between  $\pm 14$  T at fixed temperatures.

A critical ingredient for the epitaxial SnTe growth in the present experiment is the high quality of the Bi<sub>2</sub>Te<sub>3</sub> buffer layer. Figure 1(a) shows an atomic force microscopy (AFM) image of a 40-nm-thick Bi<sub>2</sub>Te<sub>3</sub> thin film grown on sapphire substrate. Large equilateral triangles with atomically flat terraces, which have a height of exactly 1 QL, can be easily recognized. An AFM image of a 30-nm-thick SnTe film grown on top of such Bi<sub>2</sub>Te<sub>3</sub> buffer layer is shown in Fig. 1(b). Triangles are still clearly seen on the surface, giving evidence for an epitaxial growth. The height of the terraces is  $\sim 0.4$  nm, which agrees with the periodicity of the rocksalt lattice along the (111) direction [Fig. 1(d)]. [An image for a larger area with clear triangular morphology is shown in the Supplemental Material (SM) [36].]

The high structural quality of both Bi<sub>2</sub>Te<sub>3</sub> and SnTe films as well as the very smooth nature of the interface between them can be judged from the Kiessig fringes [36,37] in the x-ray diffraction (XRD) measurements [Fig. 1(c); see also SM for more details]. The inset of Fig. 1(c) shows the XRD pattern for a wider angle range, in which SnTe only yields ( $2n, 2n, 2n$ ) Bragg peaks to confirm the (111) growth direction.

<sup>\*</sup>taskin@sanken.osaka-u.ac.jp

<sup>†</sup>y\_ando@sanken.osaka-u.ac.jp

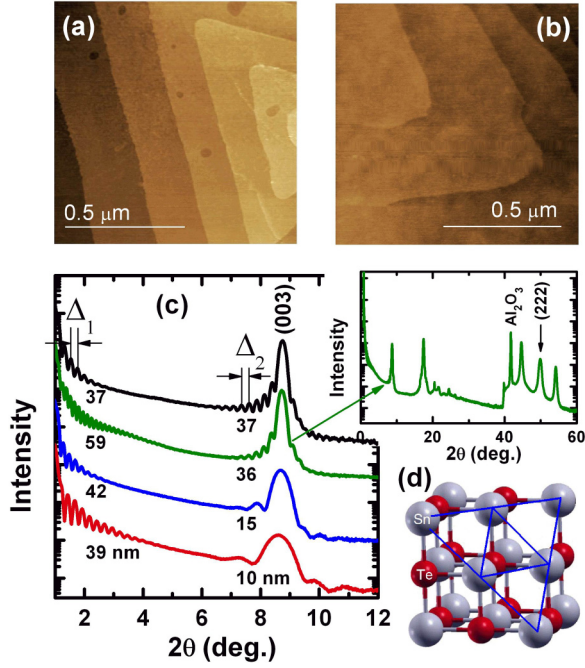


FIG. 1. (Color online) SnTe/Bi<sub>2</sub>Te<sub>3</sub> heterostructure. (a) AFM image of the Bi<sub>2</sub>Te<sub>3</sub> layer showing atomically flat terraces with 1-QL steps. (b) AFM image of the SnTe film grown on Bi<sub>2</sub>Te<sub>3</sub> buffer layer. The step height of the terraces is  $\sim 0.4$  nm. (c) Low-angle XRD patterns of a series of SnTe films grown on Bi<sub>2</sub>Te<sub>3</sub> of different thickness. The total film thickness  $d_t$  given by the distance  $\Delta_1$  of Kiessig fringes at grazing angles is shown to the left. The fringe distance  $\Delta_2$  near the (003) Bi<sub>2</sub>Te<sub>3</sub> Bragg peak gives the thickness of the Bi<sub>2</sub>Te<sub>3</sub> layer,  $d_b$ , which is shown near the peak. The SnTe layer thickness is given by  $d_t - d_b$ . Inset shows a wide-angle XRD pattern. (d) The rocksalt lattice of SnTe with its (111) plane marked by triangles.

Figure 2(a) shows the temperature dependence of the resistivity,  $\rho_{xx}(T)$ , in a 30-nm-thick SnTe film grown on 36-nm-thick Bi<sub>2</sub>Te<sub>3</sub>. There is no discernible kink in the data, suggesting that the structural phase transition observed in bulk SnTe [22,38,39] is absent in our thin films and that the mirror symmetry is kept intact down to low temperature [36]. In the magnetotransport properties, a downward cusp observed in  $\rho_{xx}(B)$  at very low fields [Fig. 2(b)] is a reflection of the weak antilocalization behavior which is expected for topological materials [40–42]. We also observe a coexistence of  $n$ - and  $p$ -type carriers in the sample which is evident from a sign change of the slope in  $\rho_{yx}(B)$  [Fig. 2(c)]. Importantly, we found that both  $\rho_{yx}(B)$  and  $\rho_{xx}(B)$  present SdH oscillations at high magnetic fields. To remove a large background and make the oscillations more visible, we employed second derivatives. Figure 2(d) shows  $d^2\rho_{yx}/dB^2$  measured in tilted magnetic fields at 1.5 K and plotted as a function of  $B \cos \theta$ , where  $\theta$  is the angle of the magnetic field from the surface normal. Since the maxima in the oscillations (marked by vertical dashed lines) appear at the same  $B \cos \theta$  upon changing  $\theta$ , the observed SdH oscillations clearly have a two-dimensional (2D) character. Note also that in our experiments, the SdH oscillations were not seen at tilting angles close to 90°, giving evidence against a three-dimensional (3D) FS as the origin of oscillations.

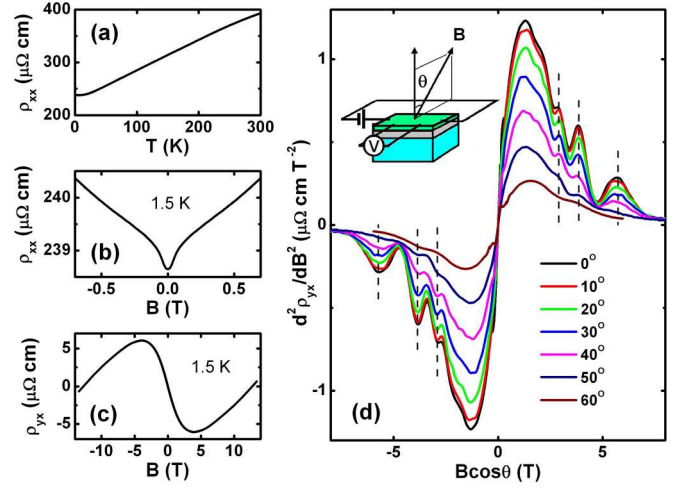


FIG. 2. (Color online) Transport properties of a 30-nm-thick SnTe film grown on a 36-nm Bi<sub>2</sub>Te<sub>3</sub> buffer layer. (a) Temperature dependence of  $\rho_{xx}$ . (b) Low-field  $\rho_{xx}(B)$  measured at 1.5 K. (c)  $\rho_{yx}(B)$  measured at 1.5 K. (d)  $d^2\rho_{yx}/dB^2$  at various angles are plotted vs  $B \cos \theta$ ; inset shows the measurement geometry. Dashed lines mark the maxima in the oscillations.

An important question is which of the  $n$ - or  $p$ -type carriers are responsible for the oscillations, and this can be answered in the following Landau-level (LL) index analysis. To properly construct the LL index plot, we use conductance  $G_{xx}$  and Hall conductance  $G_{xy}$  rather than  $\rho_{xx}$  and  $\rho_{yx}$  [4]. Figure 3(a) shows the plots of  $d^2G_{xx}/dB^2$  and  $d^2G_{xy}/dB^2$  vs  $1/B$ . The Fourier

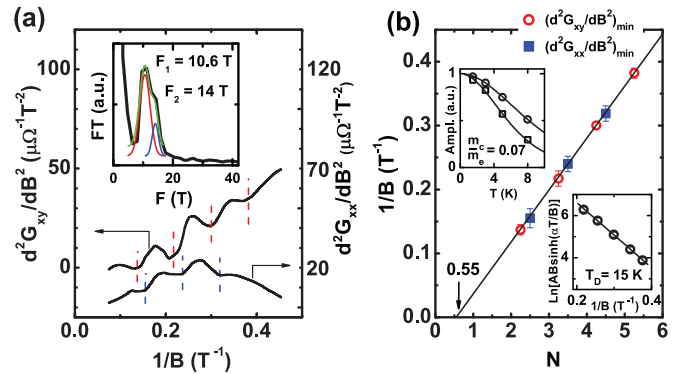


FIG. 3. (Color online) SdH oscillations. (a)  $d^2G_{xx}/dB^2$  and  $d^2G_{xy}/dB^2$  vs  $1/B$  measured at  $T = 1.5$  K and  $\theta = 0^\circ$ ; inset shows the Fourier transform of the  $d^2G_{xy}/dB^2$  oscillations revealing two close frequencies, 10.6 and 14 T (the upturn below  $\sim 5$  T is related to the background which slowly changes with  $B$ ). (b) LL index plot constructed from the minima in the oscillations of  $d^2G_{xx}/dB^2$  and  $d^2G_{xy}/dB^2$ . A half-integer index  $N + \frac{1}{2}$  is assigned to a minimum in  $d^2G_{xx}/dB^2$ . The index assignment for a minimum in  $d^2G_{xy}/dB^2$  depends on the sign of the carriers: The index  $N + \frac{1}{4}$  for electrons is consistent with the indices from  $G_{xx}$ , meaning that the SdH oscillations are produced by electrons. The solid line is a linear fitting to the data; its intercept of 0.55 on the  $N$ -index axis indicates the  $\pi$  Berry phase. Upper inset shows  $T$  dependencies of the SdH amplitudes measured at 2.67 T (squares) and 3.85 T (circles), both yielding  $m_c = 0.07m_0$ . Lower inset shows the Dingle plot for the data at 1.5 K, giving  $T_D = 15$  K.

transform of  $d^2G_{xy}/dB^2$  is shown in the inset of Fig. 3(a). Its main feature is a broadened peak with a shoulder, which can be well fitted with two Gaussians centered at frequencies of 10.6 and 14 T. The coexistence of two branches of oscillations is actually anticipated from weak beating patterns in the data. The two frequencies  $F_1 = 10.6$  T and  $F_2 = 14$  T correspond to orbits on the FSs with radii of  $k_F = 1.8 \times 10^6$  cm<sup>-1</sup> and  $2.1 \times 10^6$  cm<sup>-1</sup>, respectively. The corresponding 2D carrier densities  $n_s$  are  $2.6 \times 10^{11}$  cm<sup>-2</sup> and  $3.4 \times 10^{11}$  cm<sup>-2</sup> for each spin eigenvalue. Since the amplitude of the lower frequency oscillations is much larger than the amplitude of the higher frequency branch [see inset of Fig. 3(a)], the main contribution to the SdH oscillations is coming from the lower frequency branch; in such a case, the LL index plot constructed from weakly beating oscillations can still yield the correct phase factor for the lower frequency branch with reasonable accuracy (see SM for details). The constructed LL index plot [Fig. 3(b)] crosses the  $N$ -index axis at 0.55, which gives evidence for the Berry phase of  $\pi$  [43–45]. Also, the relative phase in the oscillations of  $d^2G_{xx}/dB^2$  and  $d^2G_{xy}/dB^2$  indicates that the carriers must be  $n$ -type (see SM for details). Therefore, the observed SdH oscillations can be concluded to be due to  $n$ -type 2D Dirac fermions bearing the  $\pi$  Berry phase. Note that even though the Bi<sub>2</sub>Te<sub>3</sub> layer contains a lot of  $n$ -type carriers (see SM), such carriers cannot be the source of the SdH oscillations, because the observed frequencies are an order of magnitude too low to represent the bulk FS of Bi<sub>2</sub>Te<sub>3</sub>.

The temperature dependence of the SdH amplitude [upper inset of Fig. 3(b)] gives the cyclotron mass  $m_c = 0.07m_0$  ( $m_0$  is the free electron mass) [46]. This value should mainly reflect the lower frequency branch of oscillations ( $F_1 = 10.6$  T) due to its dominance in the data, and we conclude that the upper limit of the Fermi velocity  $v_F (= \hbar k_F / m_c)$  of the dominant surface carriers is about  $3 \times 10^7$  cm/s. The Dingle analysis [lower inset of Fig. 3(b)] yields the Dingle temperature  $T_D$  of 15 K, from which the mean-free path of Dirac electrons  $l^{\text{SdH}} = 24$  nm and their mobility  $\mu_3^{\text{SdH}} = 2000$  cm<sup>2</sup>/V s are calculated [4]. Such a mobility is typical for best-quality SnTe films [33].

Now we discuss the origin of the observed  $n$ -type Dirac fermions. Both Bi<sub>2</sub>Te<sub>3</sub> and SnTe have topological surface states, and it is useful to consider the energy-band diagram of the heterojunction (shown in Fig. 4) formed by degenerate  $p^+$ -SnTe grown on the degenerate  $n^+$ -Bi<sub>2</sub>Te<sub>3</sub>. The lineup of the conduction and valence bands at the interface of two semiconductors is of fundamental importance for understanding the properties of the heterojunction. Essentially, there are three possibilities: straddling, staggered, and broken-gap band lineups [47] (see SM for details). The vast majority of heterojunctions have a straddling lineup with conduction- and valence-band offsets of opposite sign; in this case, when the two sides are doped with opposite types of carriers, an insulating barrier layer will be formed at the interface of such a  $p$ - $n$  junction. The same holds true for the case of a staggered lineup, in which conduction- and valence-band offsets have the same sign with a finite overlap of the gaps. The situation is different for the most exotic broken-gap lineup, in which the bottom of the conduction band of one semiconductor goes below the top of the valence band of the other semiconductor as has been shown for InAs/GaSb heterostructures [48]. In this

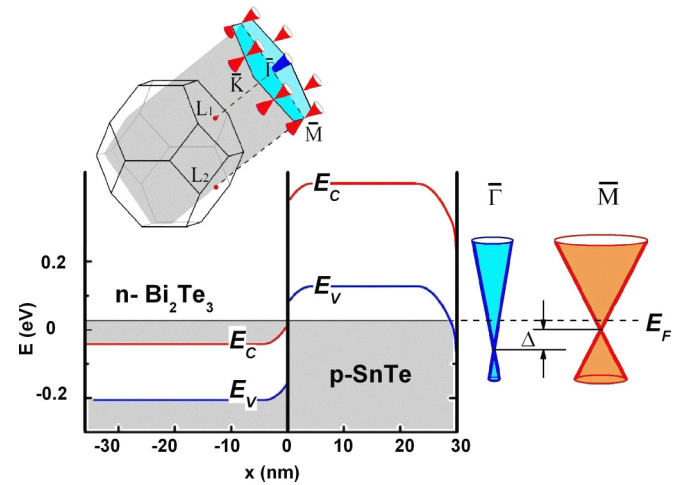


FIG. 4. (Color online) Energy-band diagram of  $n$ -Bi<sub>2</sub>Te<sub>3</sub>/ $p$ -SnTe heterojunction. The broken-gap band lineup is concluded from the  $I$ - $V$  characteristics of the heterojunction interface (see SM for details). Downward band bending on the free surface of SnTe gives rise to  $n$ -type doping of surface Dirac cones shown schematically on the right. The upper inset shows the bulk Brillouin zone of SnTe and its projection along the (111) direction to the surface Brillouin zone, which hosts two kinds of Dirac cones at  $\bar{\Gamma}$  and  $\bar{M}$ . The shaded plane is one of the three mirror planes  $\{110\}$ .

case, the system can behave as a semimetal without forming any barrier at the interface of a  $p$ - $n$  junction.

To determine which of the possible lineups is realized in our system, we measured  $I$ - $V$  curves across the interface in a sample where a part of the SnTe film has been etched away to make direct electrical contacts to both Bi<sub>2</sub>Te<sub>3</sub> and SnTe layers (see SM). We found the  $I$ - $V$  characteristics to show Ohmic behavior, which led us to conclude that the SnTe/Bi<sub>2</sub>Te<sub>3</sub> heterojunction most likely has the broken-gap lineup. In such a case, the Fermi level at the interface may lie above the bottom of the conduction band of Bi<sub>2</sub>Te<sub>3</sub> and below the top of the valence band of SnTe. Hence, while some exotic 2D state may be formed at the Bi<sub>2</sub>Te<sub>3</sub>/SnTe interface [49–51], such a state is not accessible due to the position of the Fermi level and it is unlikely that the 2D SdH oscillations come from this interface.

Another interface between Bi<sub>2</sub>Te<sub>3</sub> and sapphire is also an unlikely place for  $n$ -type Dirac fermions to reside on, because the Dirac point of the SS in Bi<sub>2</sub>Te<sub>3</sub> is situated below the top of its valence band [52]. This means that, in order for the SdH oscillations with frequencies of only 10–14 T to be observed, a very large upward band bending sufficient for creating an inversion layer would be required at the interface with sapphire. This is very unlikely and, in fact, we have never observed such low-frequency SdH oscillations in Bi<sub>2</sub>Te<sub>3</sub> films grown on sapphire.

Therefore, the only viable possibility is that the top SnTe surface has a sufficient downward band bending (Fig. 4) to host  $n$ -type Dirac fermions. Interestingly, such a band bending is naturally expected in materials with partially ionic bonding. For Sn<sup>2+</sup>Te<sup>2-</sup> films grown in the [111] direction, the stacking sequence of atomic planes is Sn<sup>2+</sup>-Te<sup>2-</sup>..., which brings about a dipole moment and leads to a diverging electrostatic energy (see SM). This situation is known as the

polar catastrophe [53] and cannot be realized in real materials; what actually happens is a partial charge compensation on the top and bottom surfaces to avoid the accumulation of electrostatic potential. In our system, the first atomic plane of the SnTe layer at the interface should be composed of  $\text{Sn}^{2+}$  and some of its positive charge is naturally compensated by  $n$ -type carriers of the  $\text{Bi}_2\text{Te}_3$  layer. On the free surface side, the termination is either with  $\text{Te}^{2-}$  or  $\text{Sn}^{2+}$  planes; since the SnTe layer begins with  $\text{Sn}^{2+}$ , the termination with  $\text{Te}^{2-}$  costs more electrostatic energy and  $\text{Sn}^{2+}$  termination is preferable (see SM). The resulting charge compensation leads to a downward band bending at the  $\text{Sn}^{2+}$ -terminated free surface as shown in Fig. 4. This offers a natural explanation of the observed  $n$ -type carriers at the free SnTe surface. Note that a strong downward band bending is also observed in ARPES experiments [54] when  $p$ -type SnTe single crystals are cleaved along the [111] direction in vacuum.

The above picture allows us to consistently understand the measured transport data. On the (111) plane of SnTe which is a TCI, there are four Dirac cones centered at four TRIMs in the surface Brillouin zone (BZ) [54,55]: one at  $\bar{\Gamma}$  and three at  $\bar{M}$  points which are projections of the four  $L$  points in the 3D BZ along the [111] direction as schematically shown in the inset of Fig. 4. The surface band calculations give different results for Te and Sn terminations [55,56]. For Te-terminated (111) surface, all Dirac points (DPs) touch the bottom of the conduction band, and it is impossible to realize  $n$ -type Dirac fermions irrespective of the position of the Fermi level. For the Sn-terminated (111) surface, on the other hand, the DPs are closer to the top of the valence band and Dirac electrons can be probed in transport experiments. Interestingly, epitaxially grown (111)-oriented films of a similar material,  $\text{Pb}_{1-x}\text{Sn}_x\text{Se}$ , were found to be preferentially terminated with Pb/Sn [57].

The observed two frequencies in the SdH oscillations are consistent with the existence of two types of Dirac cones on the free surface of SnTe reported in ARPES experiments [54]: the stronger, lower frequency branch is coming from electrons occupying the three Dirac cones at the  $\bar{M}$  points, while the weaker, higher frequency branch is coming from electrons

occupying the sole Dirac cone at the  $\bar{\Gamma}$  point. Importantly, the ARPES data show [54] that the Dirac point at  $\bar{\Gamma}$  is lower in energy than that at  $\bar{M}$ , resulting in a higher Fermi energy for the Dirac cone at  $\bar{\Gamma}$  (see Fig. 4) with a difference  $\Delta$  of  $\sim 170$  meV. It is worth noting that if oscillations were coming from the  $\text{Bi}_2\text{Te}_3$  surface, there would be only one frequency. The same is true for the SnTe/ $\text{Bi}_2\text{Te}_3$  interface, where the two Dirac cones at  $\bar{\Gamma}$  originating from SnTe and  $\text{Bi}_2\text{Te}_3$  should annihilate due to their opposite helicities [58]. The  $v_F$  of about  $3 \times 10^7$  cm/s obtained from our data may be attributed to the averaged  $v_F$  of highly anisotropic DPs at  $\bar{M}$  [56]. From  $F_1 = 10.6$  T ( $k_F = 1.8 \times 10^6$  cm $^{-1}$ ), the position of the Fermi level above the DPs at  $\bar{M}$  is estimated to be about 40 meV. For the DP at  $\bar{\Gamma}$ , according to the ARPES data [54], the Fermi velocity is much larger,  $v_F = 1.3 \times 10^7$  cm/s, and, for  $F_2 = 14$  T ( $k_F = 2.1 \times 10^6$  cm $^{-1}$ ), the position of the Fermi level would be about 180 meV above the DP. The energy difference of  $\sim 140$  meV between the two types of Dirac cones obtained in our transport experiments is close to the ARPES result of  $\Delta \sim 170$  meV, giving confidence that the observed 2D electrons indeed reside on the free surface of SnTe.

Finally, we mention that the observed SdH oscillations are prone to aging; namely, their amplitude was greatly reduced when we remeasured the sample after keeping it in nitrogen atmosphere for six months. This also supports the conclusion that the 2D oscillations are most likely coming from the free surface of SnTe. All in all, the present results demonstrate that the surface Dirac electrons residing on the (111) surface of SnTe can be accessed by transport measurements of high-quality films grown on a  $\text{Bi}_2\text{Te}_3$  buffer layer. These thin-film samples open new opportunities for experimentally exploring the physics of TCIs as well as for fabricating novel devices based on the unique nature of TCIs [59,60].

We thank J. Liu and L. Fu for helpful discussions, and M. Kishi for technical assistance with microfabrication of samples for  $I$ - $V$  measurements. This work was supported by JSPS (KAKENHI 24740237, 24540320, 25400328, and 25220708), MEXT (Innovative Area “Topological Quantum Phenomena” KAKENHI), and AFOSR (AOARD 124038).

- 
- [1] M. Z. Hasan and C. L. Kane, *Rev. Mod. Phys.* **82**, 3045 (2010).  
 [2] J. E. Moore, *Nature (London)* **464**, 194 (2010).  
 [3] X.-L. Qi and S.-C. Zhang, *Rev. Mod. Phys.* **83**, 1057 (2011).  
 [4] Y. Ando, *J. Phys. Soc. Jpn.* **82**, 102001 (2013).  
 [5] L. Fu, *Phys. Rev. Lett.* **106**, 106802 (2011).  
 [6] T. H. Hsieh, H. Lin, J. Liu, W. Duan, A. Bansil, and L. Fu, *Nat. Commun.* **3**, 982 (2012).  
 [7] Y. Tanaka, Z. Ren, T. Sato, K. Nakayama, S. Souma, T. Takahashi, K. Segawa, and Y. Ando, *Nat. Phys.* **8**, 800 (2012).  
 [8] P. Dziawa, B. J. Kowalski, K. Dybko, R. Buczko, A. Szczerbakow, M. Szot, E. Łusakowska, T. Balasubramanian, B. M. Wojek, M. H. Berntsen *et al.*, *Nat. Mater.* **11**, 1023 (2012).  
 [9] S.-Y. Xu, C. Liu, N. Alidoust, M. Neupane, D. Qian, I. Belopolski, J. D. Denlinger, Y. J. Wang, H. Lin *et al.*, *Nat. Commun.* **3**, 1192 (2012).  
 [10] A. Gyenis, I. K. Drozdov, S. Nadj-Perge, O. B. Jeong, J. Seo, I. Pletikosić, T. Valla, G. D. Gu, and A. Yazdani, *Phys. Rev. B* **88**, 125414 (2013).  
 [11] M. Safdar, Q. Wang, M. Mirza, Z. Wang, K. Xu, and J. He, *Nano Lett.* **13**, 5344 (2013).  
 [12] A. A. Taskin and Y. Ando, *Phys. Rev. B* **80**, 085303 (2009).  
 [13] A. A. Taskin, K. Segawa, and Y. Ando, *Phys. Rev. B* **82**, 121302(R) (2010).  
 [14] D.-X. Qu, Y. S. Hor, J. Xiong, R. J. Cava, and N. P. Ong, *Science* **329**, 821 (2010).  
 [15] J. G. Analytis, R. D. McDonald, S. C. Riggs, J.-H. Chu, G. S. Boebinger, and I. R. Fisher, *Nat. Phys.* **10**, 960 (2010).  
 [16] Z. Ren, A. A. Taskin, S. Sasaki, K. Segawa, and Y. Ando, *Phys. Rev. B* **82**, 241306(R) (2010).

- [17] A. A. Taskin, Z. Ren, S. Sasaki, K. Segawa, and Y. Ando, *Phys. Rev. Lett.* **107**, 016801 (2011).
- [18] B. Sacépé, J. B. Oostinga, J. Li, A. Ubaldini, N. J. G. Couto, E. Giannini, and A. F. Morpurgo, *Nat. Commun.* **2**, 575 (2011).
- [19] S. S. Hong, J. J. Cha, D. Kong, and Y. Cui, *Nat. Commun.* **3**, 757 (2012).
- [20] L. He, F. Xiu, X. Yu, M. Teague, W. Jiang, Y. Fan, X. Kou, M. Lang, Y. Wang, G. Huang *et al.*, *Nano Lett.* **12**, 1486 (2012).
- [21] J. Xiong, Y. Luo, Y. H. Khoo, S. Jia, R. J. Cava, and N. P. Ong, *Phys. Rev. B* **86**, 045314 (2012).
- [22] R. Dornhaus, G. Nimtz, and B. Schlicht, *Narrow-Gap Semiconductors* (Springer-Verlag, New York, 1983).
- [23] D. Culcer, E. H. Hwang, T. D. Stanescu, and S. Das Sarma, *Phys. Rev. B* **82**, 155457 (2010).
- [24] A. A. Taskin, S. Sasaki, K. Segawa, and Y. Ando, *Phys. Rev. Lett.* **109**, 066803 (2012).
- [25] G. Zhang, H. Qin, J. Teng, J. Guo, Q. Guo, X. Dai, Z. Fang, and K. Wua, *Appl. Phys. Lett.* **95**, 053114 (2009).
- [26] A. Richardella, D. M. Zhang, J. S. Lee, A. Koser, D. W. Rench, A. L. Yeats, B. B. Buckley, D. D. Awschalom, and N. Samarth, *Appl. Phys. Lett.* **97**, 262104 (2010).
- [27] H. D. Li, Z. Y. Wang, X. Kan, X. Guo, H. T. He, Z. Wang, J. N. Wang, T. L. Wong, N. Wang, and M. H. Xie, *New J. Phys.* **12**, 103038 (2010).
- [28] X. Chen, X.-C. Ma, K. He, J.-F. Jia, and Q.-K. Xue, *Adv. Mater.* **23**, 1162 (2011).
- [29] N. Bansal, Y. S. Kim, E. Edrey, M. Brahlek, Y. Horibe, K. Iida, M. Tanimura, G.-H. Li, T. Feng, H.-D. Lee *et al.*, *Thin Solid Films* **520**, 224 (2011).
- [30] N. Bansal, Y. S. Kim, M. Brahlek, E. Edrey, and S. Oh, *Phys. Rev. Lett.* **109**, 116804 (2012).
- [31] M. Lang, L. He, F. Xiu, X. Yu, J. Tang, Y. Wang, X. Kou, W. Jiang, A. V. Fedorov, and K. L. Wang, *ACS Nano* **6**, 295 (2012).
- [32] X. Yu, L. He, M. Lang, W. Jiang, F. Xiu, Z. Liao, Y. Wang, X. Kou, P. Zhang, J. Tang *et al.*, *Nanotechnology* **24**, 015705 (2013).
- [33] A. Ishida, T. Tsuchiya, T. Yamada, D. Cao, S. Takaoka, M. Rahim, F. Felder, and H. Zogg, *J. Appl. Phys.* **107**, 123708 (2010).
- [34] J. J. Lee, F. T. Schmitt, R. G. Moore, I. M. Vishik, Y. Ma, and Z. X. Shen, *Appl. Phys. Lett.* **101**, 013118 (2012).
- [35] A. A. Taskin, S. Sasaki, K. Segawa, and Y. Ando, *Adv. Mater.* **24**, 5581 (2012).
- [36] See Supplemental Material at <http://link.aps.org/supplemental/10.1103/PhysRevB.89.121302> for supplemental data and discussion.
- [37] U. Pietsch, V. Holý, and T. Baumbach, *High-Resolution X-Ray Scattering: From Thin Films to Lateral Nanostructures* (Springer, New York, 2004).
- [38] K. L. I. Kobayashi, Y. Kato, Y. Katayama, and K. F. Komatsubara, *Phys. Rev. Lett.* **37**, 772 (1976).
- [39] S. Katayama and D. L. Mills, *Phys. Rev. B* **22**, 336 (1980).
- [40] J. Chen, H. J. Qin, F. Yang, J. Liu, T. Guan, F. M. Qu, G. H. Zhang, J. R. Shi, X. C. Xie, C. L. Yang *et al.*, *Phys. Rev. Lett.* **105**, 176602 (2010).
- [41] J. Chen, X. Y. He, K. H. Wu, Z. Q. Ji, L. Lu, J. R. Shi, J. H. Smet, and Y. Q. Li, *Phys. Rev. B* **83**, 241304(R) (2011).
- [42] H. Steinberg, J. B. Lalöe, V. Fatemi, J. S. Moodera, and P. Jarillo-Herrero, *Phys. Rev. B* **84**, 233101 (2011).
- [43] A. A. Taskin and Y. Ando, *Phys. Rev. B* **84**, 035301 (2011).
- [44] G. P. Mikitik and Y. V. Sharlai, *Phys. Rev. B* **85**, 033301 (2012).
- [45] A. R. Wright and R. H. McKenzie, *Phys. Rev. B* **87**, 085411 (2013).
- [46] D. Shoenberg, *Magnetic Oscillations in Metals* (Cambridge University Press, Cambridge, 1984).
- [47] H. Kroemer, *Rev. Mod. Phys.* **73**, 783 (2001).
- [48] H. Sakaki, L. L. Chang, R. Ludeke, Chin-An Chang, G. A. Sai-Halasz, and L. Esaki, *Appl. Phys. Lett.* **31**, 211 (1977).
- [49] D. Soriano, F. Ortmann, and S. Roche, *Phys. Rev. Lett.* **109**, 266805 (2012).
- [50] S. Ereemeev, G. Landolt, T. V. Menshchikova, B. Slomski, Y. M. Koroteev, Z. S. Aliev, M. B. Babanly, J. Henk, A. Ernst, L. Patthey *et al.*, *Nat. Commun.* **3**, 365 (2012).
- [51] M. Koleini, T. Frauenheim, and B. Yan, *Phys. Rev. Lett.* **110**, 016403 (2013).
- [52] Y. L. Chen, J. G. Analytis, J.-H. Chu, Z. K. Liu, S.-K. Mo, X. L. Qi, H. J. Zhang, D. H. Lu, X. Dai, Z. Fang *et al.*, *Science* **325**, 178 (2009).
- [53] W. Weiss and W. Ranke, *Prog. Surf. Sci.* **70**, 1 (2002).
- [54] Y. Tanaka, T. Shoman, K. Nakayama, S. Souma, T. Sato, T. Takahashi, M. Novak, K. Segawa, and Y. Ando, *Phys. Rev. B* **88**, 235126 (2013).
- [55] J. Liu, W. Duan, and L. Fu, *Phys. Rev. B* **88**, 241303(R) (2013).
- [56] S. Safaei, P. Kacman, and R. Buczko, *Phys. Rev. B* **88**, 045305 (2013).
- [57] C. M. Polley, P. Dziawa, A. Reszka, A. Szczerbakow, R. Minikayev, J. Z. Domagala, S. Safaei, P. Kacman, R. Buczko, J. Adell *et al.*, *Phys. Rev. B* **89**, 075317 (2014).
- [58] T. Rauch, M. Flieger, J. Henk, and I. Mertig, *Phys. Rev. B* **88**, 245120 (2013).
- [59] J. Liu, T. H. Hsieh, P. Wei, W. Duan, J. Moodera, and L. Fu, *Nat. Mater.* **13**, 178 (2014).
- [60] C. Fang, M. J. Gilbert, and B. A. Bernevig, *Phys. Rev. Lett.* **112**, 046801 (2014).